Origin of 5 V Electrochemical Activity Observed in Non-Redox Reactive Divalent Cation Doped $LiM_{0.5-x}Mn_{1.5+x}O_4$ $(0 \leqslant x \leqslant 0.5)$ Cathode Materials

In Situ XRD and XANES Spectroscopy Studies

W. Wen,[a,*] B. Kumarasamy,[a] S. Mukerjee,[a,**,z] M. Auinat,[b] and Y. Ein-Eli[b,**]

[a]*Department of Chemistry and Chemical Biology, Northeastern University, Boston, MA 02115, USA*
[b]*Department of Materials Engineering, Technion-Israel Institute of Technology, Haifa 32000, Israel*

Divalent cation doped lithiated Mn spinel with Zn and Mg as cathode materials for a lithium battery are investigated and partial reversible behavior is observed at the 5 V region. The electrochemical charge and discharge potential profiles of the Zn-doped materials indicate a close relationship between the lattice energy and lattice parameters in the Zn-doped spinel system. Lithium ions extracted from octahedral sites at the 5 V plateau during the charge cycle are partially reinserted back into the tetrahedral sites during the discharge step, which contributes to the partial reversible 5 V behavior. The significant findings reported here are that the strong tetrahedral site preference of divalent nonreactive cations such as Zn and Mg force Li cations onto octahedral sites in these materials, thus resulting in electroactivity at 5 V. In situ X-ray absorption spectroscopy measurements show that the Mn *K* edge is shifted to higher energy at the 4 V plateau during charge cycle and remains unchanged at the 5 V plateau. In situ Zn *K*-edge X-ray absorption near-edge structure measurements reveal that the valence state of zinc ions is unchanged at the 5 V plateau region. In situ Mn *K*-edge extended X-ray absorption fine structure studies suggest that O^{2-} ions in the Zn-spinel lattice are partially oxidized to O^- at the 5 V plateau during the anodic process and O^- ions are reduced back to O^{2-} during the cathodic process at the 5 V plateau. The oscillations of the lattice parameters observed at the 5 V plateau region during the anodic charge step are attributed to chemical instability of O^- ions.
© 2005 The Electrochemical Society. [DOI: 10.1149/1.1997160] All rights reserved.

The current drive toward greater portability in consumer electronics and the need for more efficient power sources are a constant driving force for the scientific community to search for improved technologies and materials. One aspect of such efforts is the motivation to increase the performance of lithium ion batteries, not only from the aspect of energy density but also longer life cycle. $LiMn_2O_4$ is still recognized as a promising cathode material for the next generation of lithium batteries. It has a face-centered-cubic (fcc) spinel structure with lithium ions and Mn ions occupying tetrahedral and octahedral sites, respectively. The theoretical specific capacity of this material is 148.2 mA h/g with the characteristic two-step charge and discharge behavior, due to the formation and existence of two cubic structures during the whole charge and discharge process.[1] However, this material suffers from a strong Jahn-Teller distortion of the Mn^{3+} ions, causing a distortion of the cubic structure to a tetragonal one, leading to a drastic decrease in the cathode material's specific capacity and its life cycle.[2]

Previous reports by Tarascon and Thackarey et al.[3,4] have shown that addition of excess Li to the spinel $(Li_{1+x}Mn_{2-x}O_4)$ improves the cathode life cycle, along with a concomitant decrease in the observed capacity. Detailed analysis of this effect in the context of a Li-Mn-O phase diagram related to $LiMn_2O_4$-$Li_4Mn_5O_{12}$-$Li_2Mn_4O_9$ cathode materials has also been reported by Xia et al.[5] It was also reported that an excess of oxygen and lithium in $LiMn_{2-y}Li_yO_{4+\delta}$ is necessary to facilitate 5 V behavior, and no Mn (V) or higher Mn valance state ions are detected via quantitative analysis of the fully charged material.[6] However, an alternative view proposed by Shin et al.[7] suggests that the 5 V behavior is independent of the oxygen content. This was based on a systematic investigation of a series of oxygen excess $LiMn_{2-y}Li_yO_{4+\delta}$ and oxygen-deficient $LiMn_{2-y}Li_yO_{4-\delta}$ materials. The authors also proposed two sets of mechanisms to account for the 5 V behavior. The first one describes the oxidation of Mn ions from 4 to 5 valence state in the 5 V region and the second one describes an oxidation of oxygen ions in the

ceramic matrix. However, no spectroscopic or analytical experimental evidence has been provided so far verifying either one of the above proposed mechanisms.

It was found that doping the spinel Mn-oxide matrix with low valence state transition-metal ions resulted in a general composition of $LiM_xMn_{2-x}O_4$ which improves the cycle life of the spinel compound. Attempts to substitute Mn with elements such as Co, Mg, Cr, Ni, Fe, Ti, and Zn have been reported previously.[8-10] Initial results on these substitutions reported a lower capacity in the 4 V potential plateau compared with the $LiMn_2O_4$ spinel.[8-10] However, a significant improvement in cycle life was reported with Ni, Co,[10] and Cu substituted samples.[11,12] Later studies have shown that some of these mixed oxide spinels possess a higher voltage plateau between 4.5 and 5.0 V, as was reported with Cu,[11,12] Ni,[13-17] Cr,[14,18-20] and Fe.[16,19,21] In the case of Cr, Sigala et al.[20] attributed the two voltage plateaus to the oxidation of Mn and Cr, respectively. Zhong et al.[17] reported on Ni substitution and found that extraction of Li from $LiNi_xMn_{2-x}O_4$ (where $0 < x < 0.4$) provides an additional potential plateau at 4.6-4.7 V (in addition to the 4.1 V potential plateau). At $x = 0.5$, only the higher potential plateau was obtained, attributed to the oxidation of Ni^{2+} to Ni^{4+}. A simple model was proposed wherein the oxidation state of the compound was expressed as $LiNi_x^{2+}Mn_{1-2x}^{3+}Mn_{1+x}^{4+}O_4^{2-}$, with the capacity in the lower potential plateau varying inversely as a function of Ni substitution and the bulk of the capacity shifting to the higher potential plateau. Ohzuku produced a series of iron-doped spinels $(LiFe_xMn_{2-x}O_4)$ with a reversible capacity in the 5 V region.[19,21] Recently, Fey et al.[16] prepared and evaluated high potential cathode materials based on $LiM_xNi_{0.5-x}Mn_{1.5}O_4$ (*M* being Fe, Cu, Al, and Mg while $0 < x < 0.4$).

Zinc, cadmium, and mercury belong to group IIB (12) elements, having two *s* electrons in their outer filled *d* shells. These elements follow Cu, Ag, and Au in their electronic configurations. Copper, having filled *d* shells, loses one or two *d* electrons fairly readily to yield ions or complexes with II and III oxidation states, as was demonstrated in our previous studies with Cu-doped $LiMn_2O_4$ spinel compounds.[12,15,22] However, this is not anticipated from zinc, being a member of the group IIB (12) elements.[23] Thus, the objective of this study was to explore the influence of a cation with a

valance state of +2 from group IIB (12), which cannot be further oxidized, on the overall material electrochemistry of a doped Mn spinel compound.

Zn substituted spinel material has been investigated by the ^{7}Li solid-state nuclear magnetic resonance (NMR) method and some lithium ions were found to occupy octahedral sites, in contrast to their normal tetrahedral site occupancy in a pristine $LiMn_2O_4$.[24] Particularly, a Zn vs Li ratio of 1 and a Mn vs Li ratio of 3 in the tetrahedral and octahedral sites, respectively, are reported in the literature for $LiZn_{0.5}Mn_{1.5}O_4$ composition.[25] This suggests that Zn ions occupy tetrahedral sites in the crystal, thus forcing some fraction of lithium ions into the octahedral sites. Synchrotron X-ray diffraction (XRD) and neutron diffraction patterns of this material have been refined as a cubic structure with a space group $P2_13$.[24] The crystal structure of this material is dependent on the use of different synthetic routes. Cation ordering in the octahedral sites with a space group of $P4_332$ is reported for samples quenched from 600°C and a disordered phase with a space group $Fd3m$ if quenched from 750°C.

Recently, we reported in a short communication an unexpected 5 V behavior of low doped Zn substituted Mn spinel material of the type $LiZn_{0.25}Mn_{1.75}O_4$.[26] Here, we fully report on the synthesis and electrochemical behavior of a series of low doped Zn substituted Mn spinel materials of the type $LiZn_{0.5-x}Mn_{1.5+x}O_4$ ($0 \leq x \leq 0.5$) and on the origin of the observed 5 V behavior. The detailed mechanism has been investigated using in situ X-ray absorption near-edge structure (XANES) and XRD methods.

Experimental

Samples with the general composition of $LiZn_{0.5-x}Mn_{1.5+x}O_4$ ($0 \leq x \leq 0.5$) with $x = 0.5, 0.35, 0.325, 0.3, 0.25, 0.15$, and 0.0, and $LiMg_{0.5-x}Mn_{1.5+x}O_4$ with an x value of 0.0, 0.25, and 0.35 were prepared from the acetate salts (Li acetate, Mn acetate, and Zn and Mg acetate, Fluka) using a low-temperature sol-gel technique, described in detail elsewhere.[11,12,15] Ex situ X-ray diffraction patterns of the synthesized powdered materials were recorded with the use of a Philips X'pert Diffractometer (PW3040/60). Evaluation and examination of powder grain size and morphology were conducted with the use of a high-resolution scanning electron microscope (Hitachi S-4800).

Composite electrodes were prepared by casting (doctor blading) a slurry comprised of 80% $LiZn_{0.5-x}Mn_{1.5+x}O_4$ ($0 \leq x \leq 0.5$), 10% carbon black (Shawinigan Acetylene black), and 10% polyvinylidene di-fluoride binder with a fugitive solvent (1-methyl-2 pyrrolidinone) on an aluminum substrate (~ 5 µm), dried at 120°C under vacuum for 2 h. Electrochemical tests were performed in a PTFE T cell containing a Li metal foil anode and Li metal reference electrode, while the composite electrode served as a working electrode. Details of the electrochemical test methodology are given in Ref. 11,12. Cells were tested in the potential limits of 3.3-5.4 V at a current density of 100 µA/cm^2. Electrolyte was composed of ethylene carbonate and dimethyl carbonate mixture in a volume ratio of 1:1 containing 1 M $LiPF_6$ salt (EM Industries).

Lithiated Zn-Mn-O material with a nominal composition of $LiZn_{0.2}Mn_{1.8}O_4$ was used for in situ XRD and X-ray absorption spectroscopy (XAS) experiments with a cycling rate of C/15. Details of similar in situ spectroelectrochemical experiments in the context of XAS and XRD studies are given in detail in Ref. 12,15,22. In situ XRD was performed at Brookhaven National Laboratory (BNL, Upton, NY) at beam line X7A with a wavelength of 0.7071 Å, using a position-sensitive detector for data acquisition. The XAS data were collected at beam line X9B and X11A, using the same electrochemical cell feature as mentioned above. Zinc K-edge XAS was evaluated at X11A at BNL using fluorescence mode with a pips detector due to the low Zn concentration. Manganese K-edge XAS data were obtained at beam line X9B at BNL in a transmission mode. The XAS data were analyzed with the use of the Athena
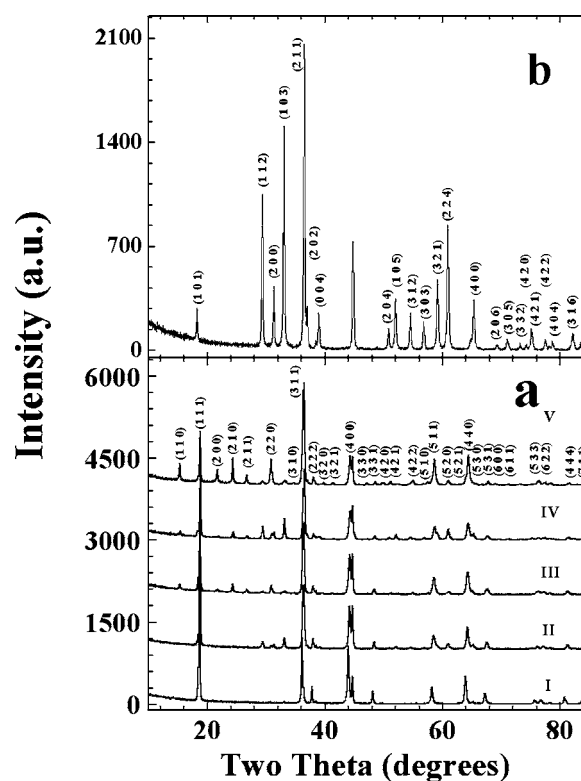

Figure 1. (a) XRD patterns of several $LiZn_{0.5-x}Mn_{1.5+x}O_4$ powder materials: (I) $x = 0.5$, (II) $x = 0.3$, (III) $x = 0.25$, (IV) $x = 0.15$, and (V) $x = 0$; (b) XRD pattern obtained from $ZnMn_2O_4$ powder.

module of the IFFFIT program.[27] The XRD data are refined using powder indexing in Cerius^2 software and CMPR program.

Results and Discussion

Materials characterization.— Powder X-ray diffraction (XRD) studies.—XRD patterns of several $LiZn_{0.5-x}Mn_{1.5+x}O_4$ powder materials are shown in Fig. 1a. XRD patterns obtained from the Zn-doped lithiated Mn-oxide materials are different from the pattern recorded from an undoped $LiMn_2O_4$ spinel (with a fcc spinel structure) due to the emergence of extra diffraction peaks. The XRD pattern for $LiZn_{0.5}Mn_{1.5}O_4$ is indexed (using a powder indexing module in the Cerius^2 program) as a cubic structure with a lattice parameter of 8.17 Å. The XRD pattern of a reference material, $ZnMn_2O_4$ which has been indexed as a tetragonal structure (due to the presence of highly Jahn-Teller active Mn^{3+} ions) with Zn ions occupying the tetrahedral sites, is also shown in Fig. 1b. Further, the intensity of some diffraction peaks, which are not observed in the $LiMn_2O_4$ XRD pattern, such as 110, 200, and 210, increases as Zn content increases. This suggests the possibility of Zn ions occupying tetrahedral sites in the crystal lattice. $LiZn_{0.5-x}Mn_{1.5+x}O_4$ materials with a Zn content of 0, 0.2, 0.25, 0.35, and 0.5 exhibit similar XRD patterns, thus suggesting the existence of similar crystal structure. The existence of additional diffraction peaks, observed in $LiZn_{0.5-x}Mn_{1.5+x}O_4$ ($0 \leq x \leq 0.5$) materials, have been indexed to a space group $P2_13$, with a primitive cubic structure instead of a face-centered-cubic spinel structure. These are evidenced by the existence of 200 and 400 planes, and an undetectable 100 plane, which suggests the existence of a 2_1 screw axis at the 100 plane. The intensity of the 110 peak increases as we move along from $LiZn_{0.2}Mn_{1.8}O_4$ to $LiZn_{0.5}Mn_{1.5}O_4$ powder material, while, as will be shown later, the electrochemical discharge capacity decreases from 100 mA h/g (recorded with $LiZn_{0.2}Mn_{1.8}O_4$) to almost 0 (recorded with $LiZn_{0.5}Mn_{1.5}O_4$).
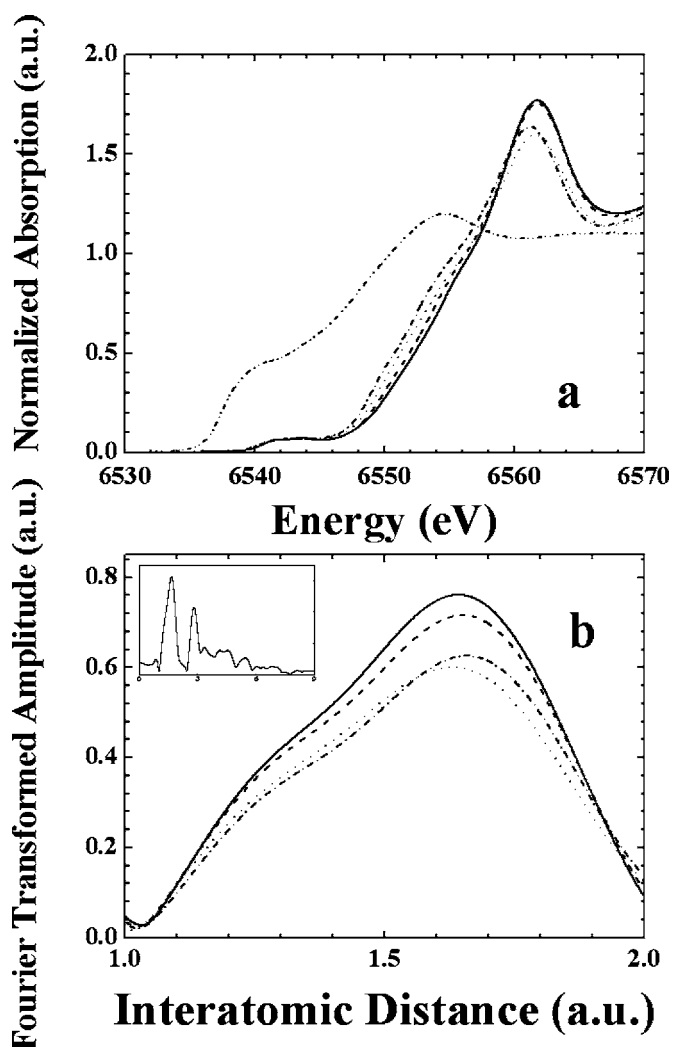
Figure 2. (a) XANES spectra obtained from $LiZn_{0.5-x}Mn_{1.5+x}O_4$:(−)$x = 0$, (---) $x = 0.25$, (......) $x = 0.3$, (--·) $x = 0.5$, and (--·-) Mn foil; (b) Fourier transformed EXAFS signal of $LiZn_{0.5-x}Mn_{1.5+x}O_4$:(−)$x = 0$, (---) $x = 0.25$, (......) $x = 0.3$, and (--·) $x = 0.5$. Inset presents a full scale spectrum of Fourier transformed EXAFS signal obtained from $LiMn_2O_4$.

Figure 3. High-resolution SEM micrographs obtained from three materials with different Zn composition of (a,b) $x = 0.5$; (c,d) $x = 0.25$; and (e,f) $x = 0.0$ in $LiZn_{0.5-x}Mn_{1.5+x}O_4$.

X-ray absorption spectroscopy (XAS).—The XANES spectra of three different Zn-doped Mn spinels, $LiMn_{1.8}Zn_{0.2}O_4$, $LiMn_{1.65}Zn_{0.35}O_4$, $LiMn_{1.5}Zn_{0.5}O_4$ and $LiMn_2O_4$, are shown in Fig. 2a. All edges of these four compounds are 10 eV above the Mn foil K edge, due to the higher oxidation state of Mn ions. It is readily seen from Fig. 2a that the oxidation state of Mn ions increases as Zn content in the ceramic compound increases, as indicated by the positive shift in the Mn K edge to higher energy levels. This is expected on the basis of charge compensation and the assumption that Zn ions are in their +2 valence state. The preedge feature at ~6540 eV indicates the transition from $1s$ orbital to 3d orbital in Mn ions, which is formally dipole-forbidden but quadrupole-allowed. This could also be explained by the hybridization of Mn 3d and oxygen 2p orbitals in the local structure. The preedge seems to be at a similar position to the K edge of the Mn foil. It is a general rule that the intensity of the preedge feature would increase with any deviation from a centrosymmetric coordination environment.[28-30] In other words, we expect to observe a large preedge feature once the coordination environment for the center ions is tetrahedral, due to the higher overlapping of the transition-metal d orbital with the coordination ions p orbital. The small magnitude of the preedge feature, observed in Fig. 2a, suggests that Mn ions are positioned in an
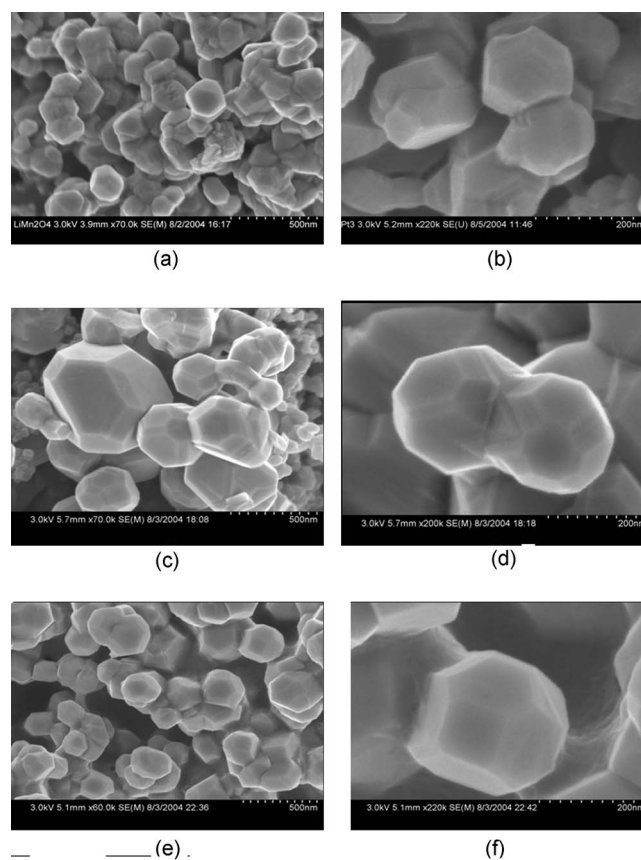
octahedral coordination environment. However, the preedge features obtained from Zn substituted materials are gradually modified: while a single preedge peak is observed in $LiMn_{1.5}Zn_{0.5}O_4$, two preedge peaks are featured in $LiMn_2O_4$. This could be the result of a decrease in the concentration of octahedral lithium ions in the crystal lattice as Zn content decreases.

Fourier transformed EXAFS signals obtained from four powdered compounds, namely $LiMn_{1.8}Zn_{0.2}O_4$, $LiMn_{1.75}Zn_{0.25}O_4$, $LiMn_{1.5}Zn_{0.5}O_4$, and $LiMn_2O_4$, are shown in Fig. 2b. The x axis indicates the bond distance while the y axis reflects the effect of coordination numbers and the Debye-Waller factor, which is the mean-square variation of the photoelectron scattering path. The first peak in the radial coordinate distance at ~1.8 Å is the Mn-O interaction and forms a part of the first coordination shell. Surprisingly, the observance of similar patterns in the Fourier transform of the EXAFS at the Mn K edge for both Zn substituted ($LiMn_{1.8}Zn_{0.2}O_4$, $LiMn_{1.75}Zn_{0.25}O_4$, and $LiMn_{1.5}Zn_{0.4}$) and undoped $LiMn_2O_4$ compounds points to a similar local environment of Mn ions in the Zn-doped materials and pristine $LiMn_2O_4$, although the XRD patterns are quite different. As shown in Fig. 2b, progressive substitution of Zn in $LiMn_2O_4$ with the general composition $LiZn_{0.5-x}Mn_{1.5+x}O_4$($0 \leq x \leq 0.5$) exhibits a corresponding increase of the first peak of the Mn K-edge EXAFS (~1.8 Å). As discussed in more detail later in the manuscript, this is related to progressive lowering of the Debye-Waller factor with increased Zn substitution, resulting in an increased order in the lattice due to higher Mn oxidation state.

High-resolution scanning electron microscopy (HRSEM).— Figure 3 presents HRSEM obtained from three samples of composition: $LiZn_{0.5-x}Mn_{1.5+x}O_4$ with $x = 0.5$, 0.25, and 0 (Fig. 3a, c, and e,
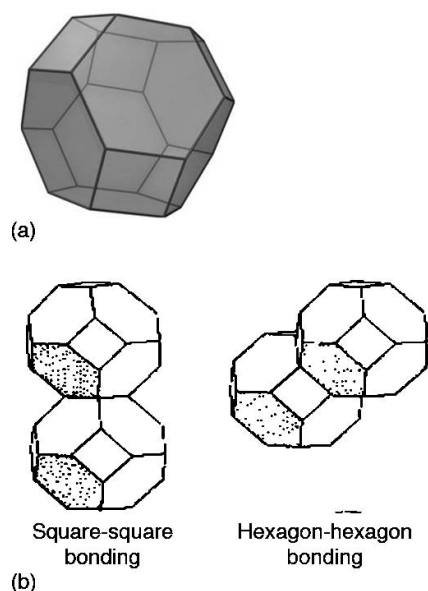
Scheme 1. (a) Truncated octahedral structure and (b) bonding possibilities.

respectively). All three materials have a truncated octahedral structure (tetradecahedra), having six squares and eight hexagons (Scheme 1a), with side lengths of 60-100 nm. Although there are two ways for cojoining two tetradecahedra units (scheme I b) and six possibilities for three tetradecahedra blocks to be linked, the SEM micrographs (Fig. 3b, d, and f) reveal that the truncated octahedrals are bonded via the hexagon facets. Observance of such well defined faceted structures is reported here for the first time for such a composition, to the best of our knowledge. These "single-crystal"-like structures are important in understanding intradomain interactions and grain fracture as a result of cycling.

Electrochemical characterizations.—Slow scan cyclic voltammetry.—Slow scan cyclic voltammetry (SSCV, scan rate of 20 μV/s) obtained from polarizing $LiZn_{0.5-x}Mn_{1.5+x}O_4$ composite electrode materials (x = 0.5, 0.35, 0.325, 0.3, 0.25, and 0.15) in ethylene carbonate-dimethyl carbonate electrolyte containing 1 M $LiPF_6$ is presented in Fig. 4a-f. The two-step charge and discharge profiles in the 4 V region of the Zn-doped ceramic compounds were resolved, as can be readily seen from Fig. 4c-f, albeit with less resolution as compared to corresponding behavior for pristine $LiMn_2O_4$, shown in Fig. 4a. The 5 V behavior is clearly observed using the SSCV method (Fig. 4c-f), which also suggests that $LiZn_{0.2}Mn_{1.8}O_4$ may have the largest discharge capacity at both the 4 and 5 V regions, on the basis of the integrated areas under the anodic and cathodic regions (Fig. 4d). The SSCV patterns and the electrochemical charge-discharge profiles of $LiZn_{0.15}Mn_{1.85}O_4$ are similar to the undoped $LiMn_2O_4$ spinel material, as the two anodic and cathodic peaks in the 4 V region are sharply resolved (Fig. 4b) compared with the two broad peaks observed with the "highly" Zn-doped materials, namely $LiMn_{1.75}Zn_{0.25}O_4$ and $LiMn_{1.65}Zn_{0.35}O_4$ (Fig. 4e and f). In addition, the 5 V behavior is barely detected upon polarizing the low doped Zn material, $LiZn_{0.15}Mn_{1.85}O_4$. This suggests that the material having a low Zn content, with x = 0.35 in $LiZn_{0.5-x}Mn_{1.5+x}O_4$, is a mixture of several phases, with the major phase being similar to the undoped pristine $LiMn_2O_4$.

It is also observed that the detected 5 V behavior recorded for the doped Zn materials is not completely reversible, as the 5 V peak in the cathodic back-scan is much smaller than the corresponding anodic peak. Surprisingly, small 5 V reversible behavior is also detected while polarizing $LiMn_2O_4$ composite electrode, as can be seen in Fig. 4a, inset, suggesting that Zn doping is not the origin of the 5 V behavior. However, the significant anodic peak in the SSCV's obtained from Zn-doped Mn oxide materials indicates that Zn doping is needed to facilitate the 5 V behavior.

Galvanostatic charge/discharge profiles.—Figure 5 presents electrochemical charge (to a potential of 5.4 V) and discharge (to a potential of 3.3 V) profiles of five $LiZn_{0.5-x}Mn_{1.5+x}O_4$ materials,

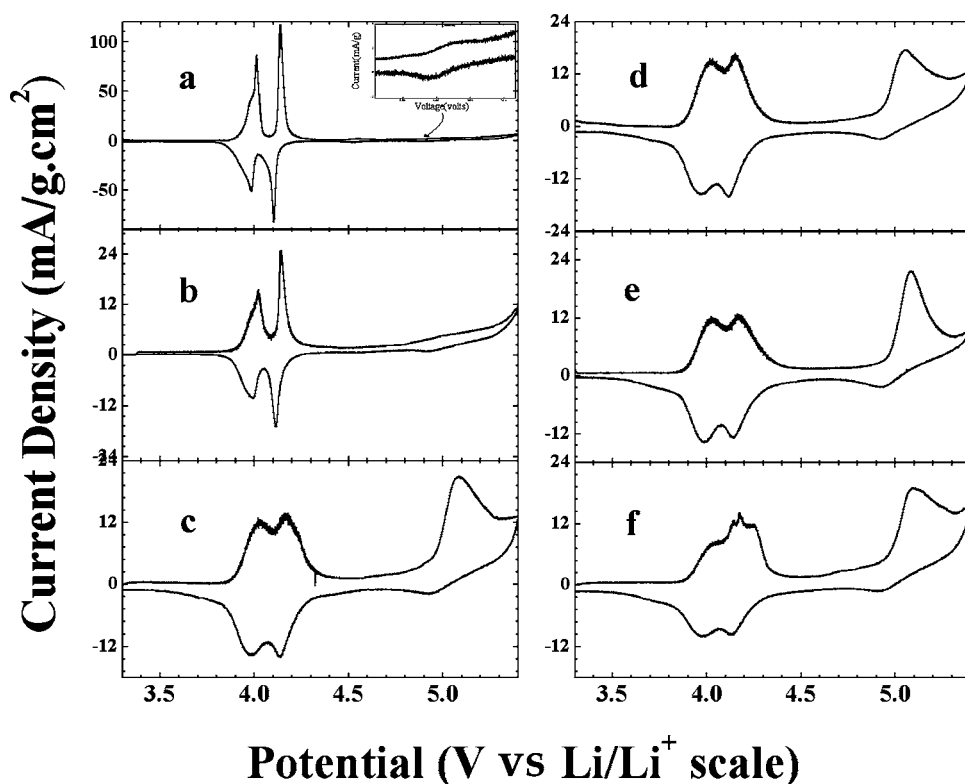**Figure 4.** Slow scan cyclic voltammetry (SSCV) obtained from polarizing $LiZn_{0.5-x}Mn_{1.5+x}O_4$ composite electrode materials at a scan rate of 20 μV/s in ethylene carbonate-dimethyl carbonate electrolyte containing 1 M $LiPF_6$. Li metal was served as both anode and reference electrodes: (a) x = 0.5, (b) x = 0.35, (c) x = 0.325, (d) x = 0.3, (e) x = 0.25, and (f) x = 0.15.
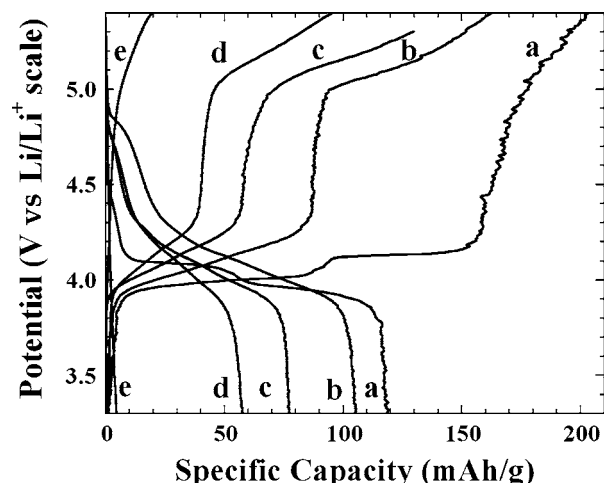
Figure 5. Galvanostatically first charge and discharge profiles of five $LiZn_{0.5-x}Mn_{1.5+x}O_4$ materials, having x values of (a) 0.5, (b) 0.3, (c) 0.25, (d) 0.15, and (e) 0.0. Cells were cycled vs Li anode in potential limits of 3.3 and 5.4 V at a current density of 0.1 mA/cm^2. Ethylene carbonate-dimethyl carbonate mixture containing 1 M $LiPF_6$ was used as electrolyte.

Figure 6. Specific capacity (mA h/g) values obtained from the first discharge step as a function of x in $LiZn_{0.5-x}Mn_{1.5+x}O_4$ materials. ■, at 4 V region; •, at 5 V region.

having x values of 0.5, 0.3, 0.25, 0.15, and 0.0. At the ultrahigh potential of 5.4 V, oxidative decomposition of the electrolyte is expected. Hence, the charge capacity recorded at this potential is much higher than the consecutive discharge capacity. Because of this, we do not present the cycle life data of these materials.

Three types of electrochemical behavior are observed:

1. The characteristic two-step charge and discharge profiles, around the 4 V region, are observed for $LiMn_2O_4$ composite electrode, indicating the existence of two cubic structures above 3 V. A smaller and almost undetectable capacity (less than a few mA h/g) at the 4.5-4.7 V potential region is detected once the electrode is discharged, in accordance with the SSCV results reported earlier (Fig. 4a).

2. Composite electrodes composed of $LiZn_{0.5-x}Mn_{1.5+x}O_4$ materials having a Zn content of 0.2, 0.25, and 0.35 possess two potential plateaus, located at 4 and 5 V, separated by a potential gap between 4.3 and 5 V. However, the two steps in the 4 V plateau are barely observed in the charge-discharge profiles obtained from polarizing these three compositions of $LiZn_{0.5-x}Mn_{1.5+x}O_4$, thus suggesting a different mechanism for structural change in the crystal lattice during the electrochemical charge and discharge process. These two regions can also be seen in the discharge step in the 4 V region. Further, the discharge capacity at 5 V is much smaller than those recorded in the charge step, suggesting a partially reversible 5 V behavior and electrolyte decomposition at these high potentials ($\sim$5.4 V). Figures 4-6 show that $LiMn_{1.8}Zn_{0.2}O_4$ composite electrode exhibits the largest 5 V discharge capacity, in addition to high 4 V discharge capacity (approximately 100 mA h/g). Figure 6 also shows that the specific discharge capacity at the 4 V region increases as the Zn content in the spinel matrix decreases, due to a decrease in the amount of Mn^{4+} ions in the crystal lattice, while the maximum 5 V discharge capacity is obtained at the relatively low Zn dopant concentration of $0.28 < x < 0.33$ in $LiZn_{0.5-x}Mn_{1.5+x}O_4$. Neither 5 V nor 4 V electrochemical activities are observed with $LiMn_{1.5}Zn_{0.5}O_4$ compound, rendered as a result of having all of the Mn in its +4 valence state, compensating for the inactive Zn divalent cation in the matrix.

3. A relatively small charge capacity, which can be attributed mainly to electrolyte oxidation and no corresponding 5 V discharge capacity, was observed for $LiMn_{1.5}Zn_{0.5}O_4$ composite electrode material. Since the charge balance for this composition mandates that all the Mn in the lattice is in an oxidation state of +4, a shift to
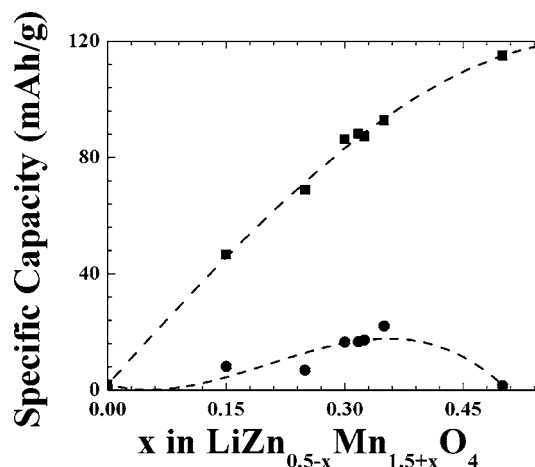
higher valence Mn as the originator of the 5 V behavior for $LiZn_{0.5}Mn_{1.5}O_4$ composite electrode can be ruled out. This argument can also be applied to the other compositions of $LiZn_{0.5-x}Mn_{1.5+x}O_4$.

In situ spectroscopy studies.—*In situ X-ray diffraction studies.*— In situ XRD studies carried out with $LiMn_{1.8}Zn_{0.2}O_4$ composite electrode as a function of charge and discharge processes are shown in Fig. 7a and b. No new diffraction peaks emerged during the charge and discharge processes, suggesting the existence of only one phase throughout. All XRD peaks obtained from polarizing $LiMn_{1.8}Zn_{0.2}O_4$ composite electrode are shifted to higher angles during the charge process (guided by the dashed vertical lines in Fig. 7), while they are shifted to lower angles in the corresponding discharge process, as the lithium ions are extracted and reinserted into the crystal lattice, respectively. This suggests a decrease in the lattice parameter during the charge process as lithium ions are
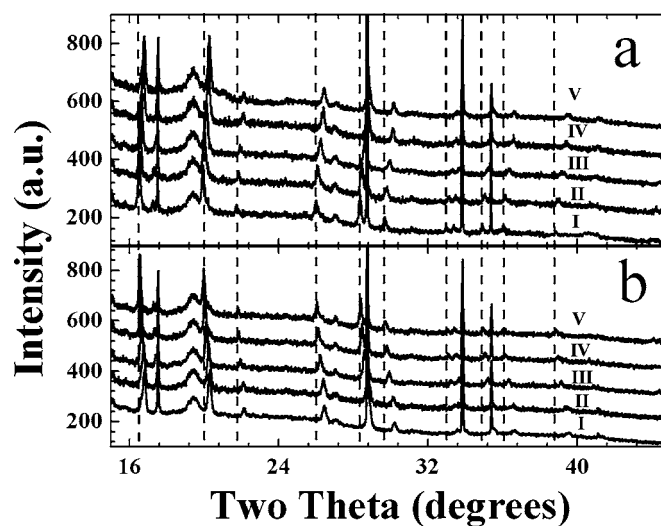

Figure 7. In situ XRD profiles obtained during galvanostatic polarization of $LiMn_{1.8}Zn_{0.2}O_4$ composite electrode: (a) electrode was charged from 3.3 to 5.4 V with a charge capacity of (I) zero (OCP state), (II) 35.4 mA h/g, (III) 74.7 mA h/g, (IV) 110.1 mA h/g, and (V) 173.03 mA h/g; (b) electrode was discharged from 5.4 to 3.3 V with a discharge capacity of (I) zero (a fully charged state), (II) 19.7 mA h/g, (III) 35.4 mA h/g, (IV) 51.1 mA h/g, and (V) 62.9 mA h/g. Vertical dashed lines serve as guides to the eye.

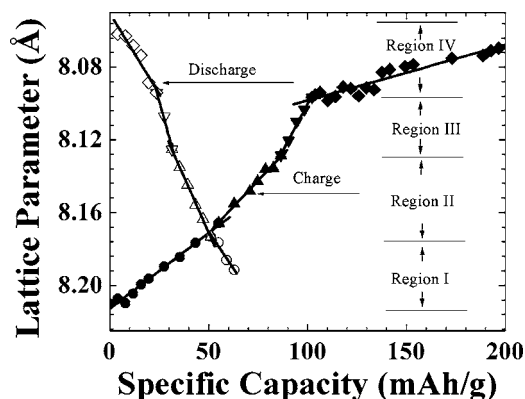**Figure 8.** A plot of lattice parameter (Å) vs specific capacity (mA h/g) values obtained during first charge and discharge steps of $LiMn_{1.8}Zn_{0.2}O_4$ composite electrode.

Figure 9. In situ Zn K-edge spectra obtained during charge step at the 5 V region from $LiMn_{1.8}Zn_{0.2}O_4$ composite electrode at different potentials: (—) 102.9 mA h/g (5.03 V), (---) 141.6 mA h/g (5.19 V), (……) 154.1 mA h/g (5.32 V), (-·-) at fully charged state (5.4 V), and (-··-) Zn reference foil.

extracted from the lattice, and an increase in the lattice parameters during the followed discharge process as lithium ions are reinserted back into the lattice.

A plot representing the lattice parameter values vs the specific capacity is shown in Fig. 8. Surprisingly, the profile of this plot is similar to the electrochemical charge and discharge curves (Fig. 5). The electrochemical potential of a cell is determined by the Gibbs free energy of the overall electrochemical reactions, which could be calculated from the Born-Harber cycle, yielding eventually the crystal lattice energy. However, the cell potential is modified not only via the amount of lithium ions inside the crystal lattice, but also by the specific site in which the lithium ion resides. Both can alter the lattice energy of the crystals. Thus, Fig. 8 suggests a close relationship between the lattice parameters and the crystal lattice energy. The lattice parameter profile in the charge cycle, presented in Fig. 8, could be divided into four regions, as shown, and is well correlated with the four regions of the electrochemical charge profiles (Fig. 5). The lattice parameter decreases from 8.211 to 8.166 Å in the first region until the charge capacity of ~55 mA h/g. In the second region, the lattice parameter decreases from 8.166 to 8.128 Å for a charge capacity of 87 mA h/g. In the third region, the lattice parameter decreases from 8.128 to 8.096 Å with the corresponding charge capacity of ~100 mA h/g. The lattice parameter continues to decrease from 8.096 to 8.068 Å in the fourth region until the charge capacity is close to 200 mA h/g. This nominal change in the lattice parameter in stage 4 is distinct from contributions in the charge capacity due to electrolyte decomposition. The rate of change in the lattice parameters is larger in the 4 V region compared with the corresponding change observed at 5 V, as indicated by linear fits in each region. Further, the change in lattice parameter at the 5 V region during charge exhibits oscillations, in contrast to the linear plots in the previous three regions.

The changes in the lattice parameter during the discharge step can also be fitted into four regions, albeit with lower resolution, as presented in Fig. 8. It is also worth noticing that the slopes of the lattice parameter change during the discharge process are significantly steeper than the slopes observed during the charging step. Again, the lattice parameter behavior within each specific potential window is also similar to the discharge profile presented in Fig. 5. This further demonstrates that the potential profile is well correlated with corresponding changes in the lattice parameters. Because the lattice energy and hence the Li extraction potential are related to the lattice parameter, the higher potential activity at 5 V region could be attributed to the extraction of lithium ions from octahedral sites which possess higher lattice energy than the tetrahedral lithium ions in the crystal lattice. The data represented in Fig. 8 suggest that a
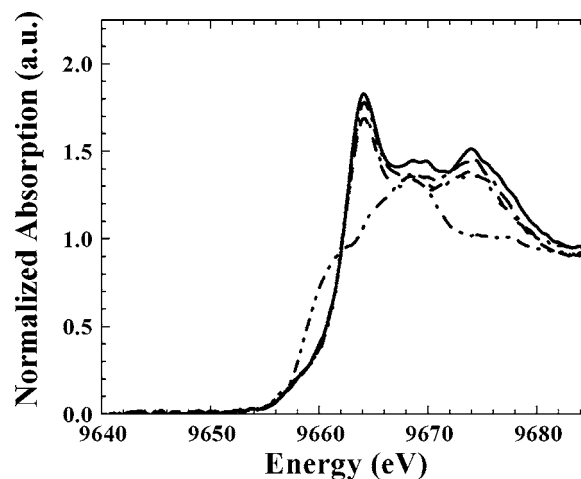
compound is more readily susceptible to structural changes when lithium ions are extracted from tetrahedral sites as compared to octahedral sites.

In situ XANES measurements.—In situ Zn K-edge XANES spectra obtained during the charge cycle are shown in Fig. 9. No shifts toward higher energies are observed in the zinc K-edge XANES spectra at the 5 V region during the charge step; such a shift is expected for any positive change in Zn valence states. No preedge feature due to a $3d^{10}$ configuration of the Zn^{2+} ion is observed, as well. The preedge feature presents the transition from $1s$ orbital to $3d$ orbital, which is dipole-forbidden but quadrupole-allowed. The absence of a preedge feature in the fully charged state suggests that no Zn^{3+} ions exist in the ceramic matrix; otherwise, a preedge feature should be expected for a $3d^9$ configuration.

The intensity of the preedge is expected to be high for tetrahedral Zn^{3+} ions. This is consistent with the existence of 5 V behavior in $LiMn_2O_4$. It is thus concluded that the origin of the 5 V behavior in a $LiZn_{0.5-x}Mn_{1.5+x}O_4$ material system is different from that of other transition-metal substituted spinel materials such as $Cu^{12,22}$ and $Ni,^{16,17}$ where charge compensation due to valence change involving the transition metals completely accounts for the 5 V behavior.

In situ Mn K-edge XANES profiles obtained during charge in the 4 V region are shown in Fig. 10a. The Mn K edge is shifted to a higher energy level at the 4 V region, indicating an increase in Mn oxidation state, in order to compensate for the extraction of lithium ions from the crystal lattice. However, the corresponding XANES spectra obtained during charge at the 5 V plateau exhibit no shifts in the main Mn K-edge peak, as shown in Fig. 10b. A close examination of the preedge region of these spectra reveals a continuous enhancement of intensity in both the 4 and 5 V regions. Since these preedge features emanate as a result of a hybridization p-d state enabling quadrupole-allowed transitions, an increase in preedge peak intensity suggests an increased distortion of the Mn-O coordination in both the 4 and 5 V regions. It can be conjectured that in the 4 V region, the presence of Zn in tetrahedral sites forces some Li ions into octahedral positions, creating an environment in which Mn-O distortions could occur. This is supported somewhat by previous studies on chemical intercalation of $LiMn_2O_4$ and a Li-rich analog $Li_{4/3}Mn_{5/3}O_4.^{31}$ One of the explanations of the changes in the preedge features, especially in the 5 V region (where the main peak does not change), could be due to the oxidation of the O^{2-} ions to O^- ions in the 5 V region. The fully charged state is thus correlated to a locally distorted octahedral coordination environment near the Mn^{4+} ions.
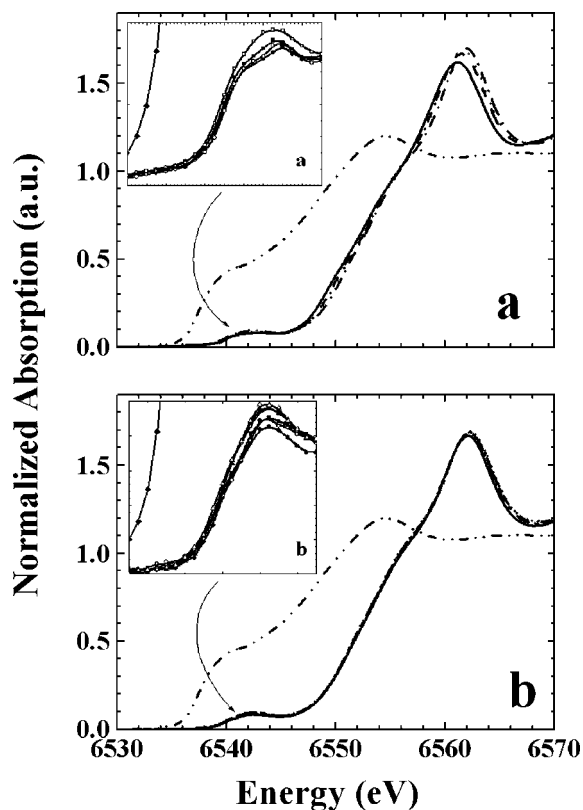
Figure 10. In situ Mn K-edge XANES profiles obtained during charge step of $LiMn_{1.8}Zn_{0.2}O_4$ composite electrode: (a) at the 4 V region with a charge capacity of (—) zero charge (OCP = 3.3 V), (---) 29.2 mA h/g (4.07 V), (……) 44.8 mA h/g (4.15 V), (-··-) 74.5 mA h/g (4.83V), and (-···-) a Mn reference foil. The preedge is shown in the inset, (♦) Mn foil, (•) zero charge (OCP = 3.3 V), (○) 29.2 mA h/g (4.07 V), (■) 44.8 mA h/g (4.15 V), and (□) 74.5 mA h/g (4.83 V); and (b) at the 5 V region with a charge capacity of (—) 82.2 mA h/g (4.97 V), (---) 89.9 mA h/g (5.01 V), (……) 97.5 mA h/g (5.05 V), (-··-) 105.2 mA h/g (5.08 V), (------) 112.9 mA h/g (5.09V), (·········) a fully charged state (5.4 V), and (-···-) a Mn reference foil. The preedge is shown in the inset. (♦) Mn foil, (•) 82.2 mA h/g (4.97 V), (○) 89.9 mA h/g (5.01 V), (■) 97.5 mA h/g (5.05 V), (□) 105.2 mA h/g (5.08 V), (▲) 112.9 mA h/g (5.09V), and (△) a fully charged state (5.4 V).

Figure 11. In situ Mn K-edge XANES spectra obtained during discharge step of $LiMn_{1.8}Zn_{0.2}O_4$ composite electrode: (a) at the 5 V region with a discharge capacity of (—) 7.7 mA h/g (4.79 V), (---) 15.4 mA h/g (4.45 V), and (……) 23.2 mA h/g (4.23 V). The preedge is shown in the inset. (♦) Mn foil, (•) 7.7 mA h/g (4.79 V), (○) 15.4 mA h/g (4.45 V), and (■) 23.2 mA h/g (4.23 V); and (b) at the 4 V region with a discharge capacity of (—) 52.8 mA h/g (4.03 V), (---) 61.3 mA h/g (3.98 V), (……) 92.2 mA h/g (3.73 V), (-··-) at fully discharged state (3.3 V), and (-···-) a Mn reference foil. The preedge is shown in the inset. (♦) Mn foil, (•) 52.8 mA h/g (4.03 V), (○) 61.3 mA h/g (3.98 V), (■) 92.2 mA h/g (3.73 V), and (□) fully discharged state (3.3V).

In situ XANES spectra at the 5 and 4 V regions in the discharge step are shown in Fig. 11a and b, respectively. A similar lack of any peak shifts in the 5 V region and the reverse shift of the peak positions in the 4 V plateau are observed. A similar reversible change is also observed in the preedge feature. This behavior observed in the 5 V region shows some reversibility with regard to Mn local environment related to Mn-O interactions.

In situ Fourier transformed EXAFS.—Correlation of the short-range atomic order by EXAFS with the lattice arrangement in the context of the spinel structure of $LiMn_2O_4$ has been described earlier.[31] Briefly, in the unit cell of $LiMn_2O_4$ (space group $Fd3m$), the oxygen atoms form a cubic close-packed array occupying 32e sites, while the Mn atoms occupy the 16d sites (half of the octahedral holes) and the Li atoms occupy one-eighth of the tetrahedral holes (8a sites). From a short-range atomic order perspective of an absorber and scatterer, the first-shell interactions around the Mn atoms (Mn K-edge EXAFS) are six oxygen atoms (octahedrally coordinated) followed by a second coordination shell of six Mn atoms in the neighboring octahedra around the central MnO_6 octahedron. An EXAFS spectrum taken at room temperature is expected to primarily reflect these interactions as the dominant ones. Interactions from more distant oxygen and Li neighbors are expected to be negligible. Those from more distant Mn atoms could provide some sig-
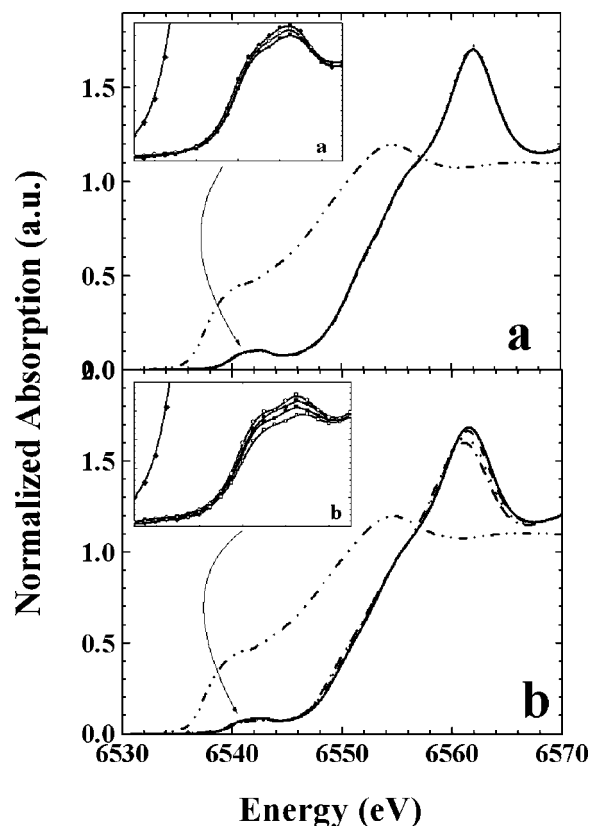
nificant interactions due to the phenomenon of forward focusing, which accounts for the appearance of peaks in the radial coordinate distances of 4-5 Å and at 8 Å.

The Fourier transforms of the EXAFS at the Mn K edge are shown in Fig. 12 and 13, representing in situ spectra for charge and discharge of $LiMn_{1.8}Zn_{0.2}O_4$. These EXAFS spectra when correlated with crystallographic features represent the Mn-O interactions of the first coordination shell at approximately 1.8 Å (without phase correction) and the Mn-Mn interactions of the second coordination shell reflecting the six octahedral Mn atoms (see the inset). Previous reports on the intercalation and deintercalation of Li in $LiMn_2O_4$ (chemically rendered) have indicated that removal of Li from the lattice causes a decrease in both the Mn-O and Mn-Mn distances, in good agreement with X-ray crystallographic data, while this was also shown to be completely reversible.[31]

Typically, the amplitude of the Fourier transform of the EXAFS signal is effected directly by the change in coordination number and inversely by the Debye-Waller factor. The Debye-Waller factor is, however, composed of both static and dynamic (thermal disorder) terms. The latter reflects the extent of interatomic dislocations, while the former represents a measure of sample purity. An earlier report on the effect of charge and discharge in the context of $LiMn_2O_4$ shows that deintercalation of Li during charge from the spinel structure causes the amplitude of the Fourier transform to increase.[32] This is also shown to be reversible, hence a concomitant decrease in the
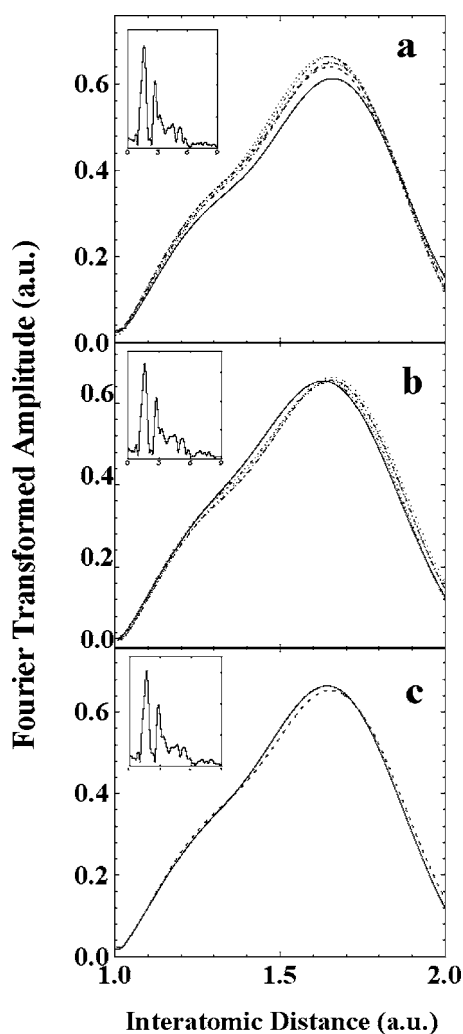
Figure 12. In situ Mn *K*-edge Fourier transformed EXAFS signals obtained during charge step of $LiMn_{1.8}Zn_{0.2}O_4$ composite electrode: (a) Signal was obtained at the 4 V region with a charge capacity of (—) 7.7 mA h/g (3.96 V), (---) 29.2 mA h/g (4.07 V), (……) 44.8 mA h/g (4.15 V), (-··-) 60.1 mA h/g (4.22 V), (-···-) 67.8 mA h/g (4.30 V), and (------) 74.5 mA h/g (4.83 V); (b) signal was obtained at the 5 V region with a charge capacity of (—) 82.2 mA h/g (4.97 V), (---) 89.9 mA h/g (5.01 V), (……) 97.5 mA h/g (5.05 V), (-··-) 105.2 mA h/g (5.08 V), (-···-) 112.9 mA h/g (5.09 V), and (------) fully charged state (5.4 V); (c) expansion view of Fig. 11b; a comparison between EXAFS signal at (—) charged 74.5 mA h/g (4.83 V) and (---) a fully charged state (5.4 V). Insets present full-scale spectra of Fourier transformed EXAFS signal.

Figure 13. In situ Mn *K*-edge EXAFS spectra obtained during a discharge step of $LiMn_{1.8}Zn_{0.2}O_4$ composite electrode at (a) the 5 V region with a discharge capacity of (—) 7.7 mA h/g (4.79 V), (---) 15.4 mA h/g (4.45 V), and (……) 23.2 mA h/g (4.23 V); and (b) the 4 V region with a discharge capacity of (—) 23.2 mA h/g (4.23 V), (---) 52.8 mA h/g (4.03 V), (……) 61.3 mA h/g (3.98 V), (-··-) 92.2 mA h/g (3.73 V), and (-···-) a fully discharge state (3.3 V). Insets present full-scale spectra of Fourier transformed EXAFS signal.

amplitude is observed during intercalation as a consequence of electrochemical discharge. This change in the amplitude of the Fourier transform has been correlated primarily to the change in the Debye-Waller factor linked to thermal disorder, hence an increase of the Fourier transform amplitude reflects a decrease in the Debye-Waller factor, as observed previously for $LiMn_2O_4$,[32] which was accounted for on the basis of greater order in the lattice due to an increase in the Mn oxidation state (toward +4 valency) and a more ordered local coordination environment of γ-MnO_2. In the case of Zn substitution, the Mn oxidation states are significantly affected and are higher than the threshold limit of 3.5 (below which local disorder is rendered due to the Jahn-Teller effect). Hence, a greater substitution of Zn is expected to increase the amplitude of the Mn-O peaks (~ 1.8 Å), as seen previously in Fig. 2.

Removal of Li during charge from the lattice in the 4 V region is shown in Fig. 12a. As expected, there is an increase in the amplitude
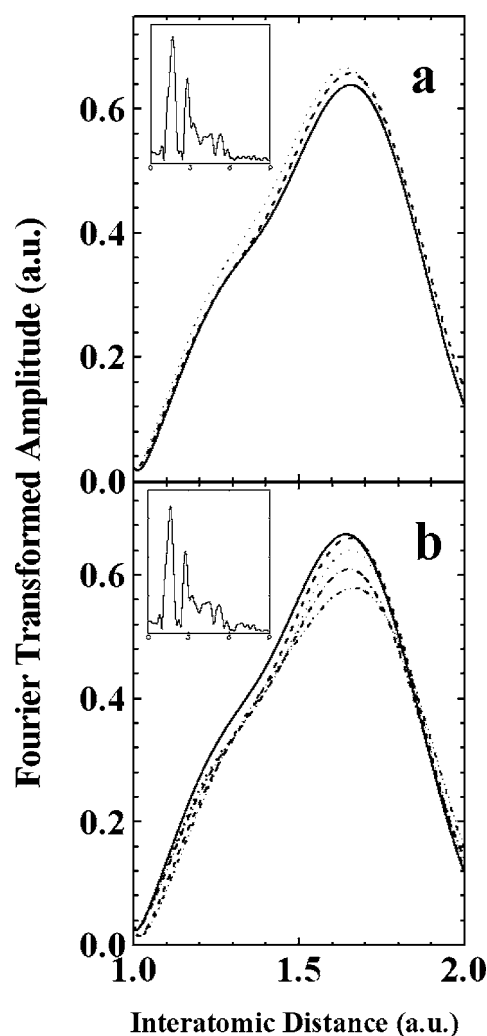
of the Mn-O Fourier transforms as a function of charge in the 4 V region. Comparison of the results presented in Fig. 12 and 13 with previous reports shows that the extent of changes in the magnitude of the Fourier transforms as a function of charge (Fig. 12a) and discharge (Fig. 13a) is relatively small for the Zn substituted sample as compared to the nondoped pure $LiMn_2O_4$ spinel. This is shown in terms of the comparison presented in Fig. 2 and is in agreement with the correlation with Mn oxidation state changes as a function of Zn substitution.

However, comparison of the corresponding magnitudes in the Fourier transforms of the Mn *K*-edge EXAFS spectra in the 5 V region exhibits a reverse trend, albeit small. This reverse trend comprised of an increase in the Debye-Waller factor as evidenced by a lowering of the magnitude of the Mn-O Fourier transform during charge (Fig. 12b) and the corresponding reverse effect during discharge related to a lowering of the Debye-Waller factor is shown in Fig. 13a. Such behavior in the 5 V region can be accounted for on the basis of a decrease in the ionic characteristics of Mn-O interaction as a consequence of a partial change of O^{2-} ions to O^- ions, which would cause an increase in the Debye-Waller factor as a
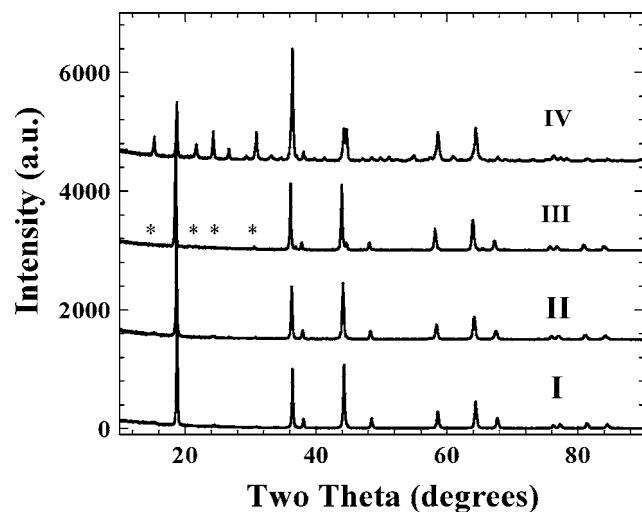
Figure 14. XRD patterns of several $LiMg_{0.5-x}Mn_{1.5+x}O_4$ powder materials: (I) $x = 0.35$, (II) $x = 0.25$, (III) $x = 0.0$, and (IV) XRD pattern obtained from $LiZn_{0.5}Mn_{1.5}O_4$ powder is shown for comparison. Some diffraction peaks due to a primitive cubic lattice are marked by asterisks.

result of a decrease in the Mn-O interactions. The fully charged material could be described using a formula of $[Zn_{0.2}]^{2+}[Mn_{1.8}]^{4+}[O_{3.6}]^{2-}[O_{0.4}]^-$, and the average oxidation state of the oxygen ions is -1.9. The reversibility of this effect is manifested in the reverse trends seen in Fig. 13a. The presence of unstable O^- in the lattice during charge in the 5 V region is expected to be accompanied by electrolyte oxidation.

Secondary reactions during the upper potential charge step, due to the presence of unstable monovalent oxygen ions at high potentials, could result in disproportionate reactions, according to the following set of equations

$$2O^- + 2Mn^{+4} \rightarrow O_2 + 2Mn^{+3} \qquad [1]$$

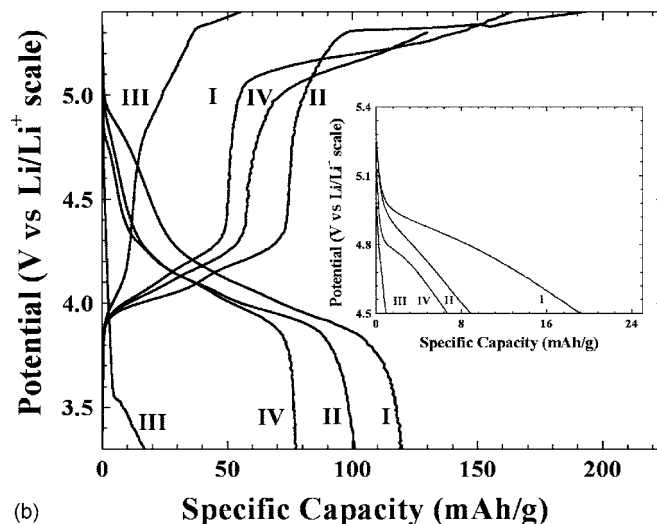$$O^- + (electrolyte) \rightarrow O^{-2} + (electrolyte)^+ \qquad [2]$$
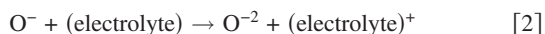
In addition, under the extreme oxidizing potentials it is more likely to expect that a major by-product of the alkyl carbonate electrolyte oxidation would be protons.[33,34] The produced protons at the electrode surface can initiate a cation exchange for Li ions in the electrode, as was proposed by Robertson et al.[35] exploring the electrochemical behavior of Li_2MnO_3. Thus, the rapid degradation in the observed capacity can be accounted for by two major processes occurring upon charging to the extremely high potential: oxygen loss and proton/Li ion exchange. The coordination number of the Mn ions is expected to decrease due to the oxygen evolution as described in Eq. 2 and will also contribute to the decrease of the magnitude of the Mn-O interaction in the Fourier transformed EXAFS signals.

The electrochemical behavior of $LiMg_{0.5-x}Mn_{1.5+x}O_4$.—In order to evaluate the influence of non-Redox divalent cation introduced into the spinel matrix on the electrochemical activity of the Mn spinel materials at the 5 V region and to establish that the nonactive redox divalent cation forces some Li ions to reside in octahedral sites and in return the nonactive divalent cation resides in the original lithium tetrahedral sites, we also studied and evaluated lithiated Mn spinels doped materials with magnesium bearing a general formulation of $LiMg_{0.5-x}Mn_{1.5+x}O_4$ $(0.0 \leq x \leq 0.5)$. $LiMg_{0.5-x}Mn_{1.5+x}O_4$ $(0.0 \leq x \leq 0.5)$ materials were synthesized from the acetate salts as outlined in the Experimental section. The XRD patterns obtained from $LiMg_{0.5-x}Mn_{1.5+x}O_4$ $(x = 0.35, 0.25,$ and $0.5)$ and $LiZn_{0.5}Mn_{1.5}O_4$ are shown in Fig. 14, I, II, III, and IV, respectively. It is noted that some new diffraction peaks (marked by asterisks in Fig. 14) appear in the spectra of the heavily Mg-doped materials, which are also

(a)

(b)
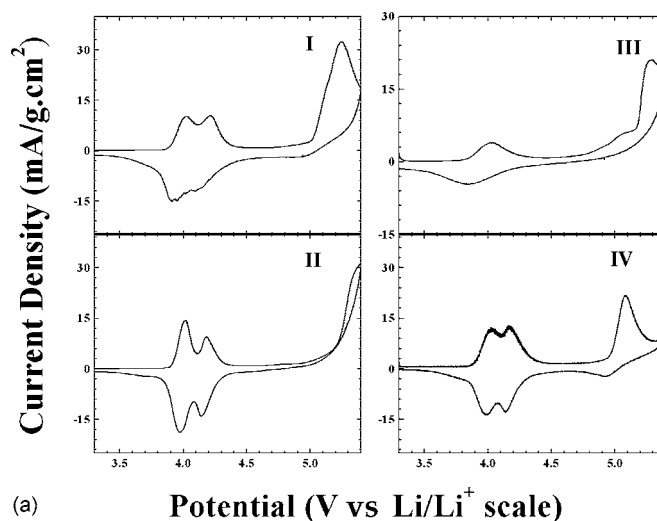
Figure 15. (a) Slow scan cyclic voltammetry (SSCV) obtained from polarizing $LiMg_{0.5-x}Mn_{1.5+x}O_4$ composite electrode materials at a scan rate of 20 μV/s in ethylene carbonate-dimethyl carbonate electrolyte containing 1 M $LiPF_6$. (I) $x = 0.35$, (II) $x = 0.25$, (III) $x = 0$, and (IV) SSCV obtained from polarizing $LiZn_{0.25}Mn_{1.75}O_4$ composite electrode materials at the same conditions. Li metal served as both anode and reference electrodes. (b) Galvanostatic first charge and discharge profiles of $LiMg_{0.5-x}Mn_{1.5+x}O_4$ materials, having x values of (I) 0.35, (II) 0.25, (III) 0, and (IV) first galvanostatic charge and discharge cycle of $LiZn_{0.25}Mn_{1.75}O_4$ material, are shown for comparison. Cells were cycled vs Li anode in potential limits of 3.3 and 5.4 V at a current density of 0.1 mA/cm^2. Ethylene carbonate-dimethyl carbonate mixture containing 1 M $LiPF_6$ was used as electrolyte.

present at almost similar positions to that of $LiZn_{0.5}Mn_{1.5}O_4$. Similar results are also reported in the literature[25,36,37] and $LiMg_{0.5}Mn_{1.5}O_4$ is refined to a primitive cubic structure with a space group of $P4_332$.

The electrochemical behavior recorded from polarizing the Mg-doped spinel materials is shown in Fig. 15a (slow scan cyclic voltammetry) and 15b (first galvanostatic charge and discharge between the potential limits of 3.3 and 5.4 V). This figure also presents a comparison of the electrochemical activity recorded from electrochemically polarizing doped Mg and Zn materials. As can be seen, a 5 V activity is also detected with the low doped Mg materials. The pronounced 5 V activity was detected to be with the $LiMg_{0.15}Mn_{1.85}O_4$ composition. Thus, the doping of the Mn spinel with nonreactive divalent cation causes the appearance of a 5 V activity. Magnesium as an additive in lithiated Mn spinel oxide deserves more scientific attention in light of these recent results. Thus,

extending our view on the role of non-Redox divalent cation in the Mn oxide spinel matrix has been demonstrated by doping Mg instead of Zn.

Conclusions

Partial reversible behavior of $LiZn_{0.5-x}Mn_{1.5+x}O_4$ group materials is observed at the 5 V region. As seen from in situ XRD spectroscopy studies, the diffraction peaks are shifted to a higher angle in the charge process and shifted backwards during the discharge cycle, while lithium ions are extracted from and reinserted into the crystal lattice, respectively. The lattice parameters vs discharge capacity plot resembles the electrochemical charge and discharge potential profiles and implicate a close relationship between lattice energy and lattice parameters in the Zn-doped spinel system. Lithium ions extracted at 5 V during the charge cycle are partially reinserted back into the tetrahedral sites during the discharge step, which probably contributes to the partial reversible 5 V behavior. The significant findings reported here are that the strong tetrahedral site preference of a divalent nonreactive cation such as Zn and Mg forces the Li cation onto octahedral sites in these materials, thus causing electroactivity at the 5 V region from the displaced Li in the 16d sites of the spinel. In situ XAS measurements show that the Mn *K* edge is shifted to high energy at the 4 V region during the charge cycle and remains unchanged at the 5 V region. In situ Zn *K*-edge XANES measurements reveal that the zinc ion valance state was not changed at the 5 V region. In situ Mn *K*-edge EXAFS studies suggest that O^{2-} ions in the Zn-spinel lattice are being partially oxidized to O^- at the 5 V plateau during the anodic process and that some of the unstable O^- ions are being reduced back to O^{2-} during cathodic process at 5 V. The oscillations of the lattice parameters observed at the 5 V region during the anodic charge step are attributed to the chemical instability of O^- ions, leading to electrochemical disproportion reactions.

References

1. T. Ohzuku, M. Kitagawa, and T. Hirai, *J. Electrochem. Soc.*, **137**, 769 (1990).
2. M. M. Thackeray, Y. Shao-Horn, A. J. Kahaian, K. D. Kepler, E. Skinner, J. T. Vaughey, and S. A. Hackney, *Electrochem. Solid-State Lett.*, **1**, 7 (1998).
3. J. R. Gummow, A. de Kock, and M. M. Thackeray, *Solid State Ionics*, **69**, 59 (1994).
4. R. H. Arias, K. Wood, and E. H. Alanis, *Environmental Studies*, **11**, 167 (2004).
5. Y. Xia and M. Yoshio, *J. Electrochem. Soc.*, **144**, 4186 (1997).
6. X. Wang, N. Iltchev, H. Nakamura, H. Noguchi, and M. Yoshio, *Electrochem. Solid-State Lett.*, **6**, A99 (2003).
7. Y. Shin and A. Manthiram, *Electrochem. Solid-State Lett.*, **6**, A249 (2003).
8. J. M. Tarascon, E. Wang, F. K. Shokoohi, W. R. McKinnon, and S. Colson, *J. Electrochem. Soc.*, **138**, 2859 (1991).
9. R. Bittihn, R. Herr, and D. Hoge, *J. Power Sources*, **43**, 223 (1993).
10. L. Guahua, H. Ikuta, T. Uchida, and M. Wakihara, *J. Electrochem. Soc.*, **143**, 178 (1996).
11. Y. Ein-Eli and W. F. Howard, Jr., *J. Electrochem. Soc.*, **144**, L205 (1997).
12. Y. Ein-Eli, W. F. Howard, Jr., S. H. Lu, S. Mukerjee, J. McBreen, J. T. Vaughey, and M. M. Thackeray, *J. Electrochem. Soc.*, **145**, 1238 (1998).
13. J. H. Kim, C. S. Yoon, S. T. Myung, J. Prakash, and Y. K. Sun, *Electrochem. Solid-State Lett.*, **7**, A216 (2004).
14. Y.-S. Lee, Y. M. Todorov, T. Konishi, and M. Yoshio, *ITE Letters on Batteries, New Technologies & Medicine*, **1**, 883 (2000).
15. S. Mukerjee, X. Q. Yang, X. Sun, S. J. Lee, J. McBreen, and Y. Ein-Eli, *Electrochim. Acta*, **49**, 3373 (2004).
16. G. T.-K. Fey, C.-Z. Lu, and T. P. Kumar, *J. Power Sources*, **115**, 332 (2003).
17. Q. Zhong, A. Banakdarpour, M. Zhang, Y. Gao, and J. R. Dahn, *J. Electrochem. Soc.*, **144**, 205 (1997).
18. A. Le Gal La Salle, A. Verbaere, Y. Piffard, and D. Guyomard, *NATO ASI Ser., Ser. 3*, **85**, 241 (2000).
19. T. Ohzuku, S. Takeda, and M. Iwanaga, *J. Power Sources*, **81-82**, 90 (1999).
20. C. Sigala, D. Guyomard, A. Verbaere, Y. Piffard, and M. Tournoux, *Solid State Ionics*, **81**, 167 (1995).
21. T. Ohzuku, K. Ariyoshi, S. Takeda, and Y. Sakai, *Electrochim. Acta*, **46**, 2327 (2001).
22. S. Mukerjee, X. Q. Yang, X. Sun, S. J. Lee, J. McBreen, and Y. Ein-Eli, *Mater. Res. Soc. Symp. Proc.*, **548**, 149 (1999).
23. F. A. Cotton and G. Wilkinson, *Advanced Inorganic Chemistry*, John Wiley & Sons, New York (1988).
24. Y. J. Lee, S.-H. Park, C. Eng, J. B. Parise, and C. P. Grey, *Chem. Mater.*, **14**, 194 (2002).
25. G. Blasse, *J. Inorg. Nucl. Chem.*, **26**, 1473 (1964).
26. Y. Ein-Eli, W. Wen, and S. Mukerjee, *Electrochem. Solid-State Lett.*, **8**, A141 (2005).
27. M. Newville, *J. Synchrotron Radiat.*, **8**, 322 (2001).
28. T. E. Westre, P. Kennepohl, J. G. DeWitt, B. Hedman, K. O. Hodgson, and E. I. Solomon, *J. Am. Chem. Soc.*, **119**, 6297 (1997).
29. P. A. O'Day, J. J. Rehr, S. I. Zabinsky, and G. E. Brown, Jr., *J. Am. Chem. Soc.*, **116**, 2938 (1994).
30. G. G. Li, F. Bridges, and C. H. Booth, *Phys. Rev. B*, **52**, 6332 (1995).
31. B. Ammundsen, D. J. Jones, J. Roziere, and G. R. Burns, *Chem. Mater.*, **8**, 2799 (1996).
32. Y. Shiraishi, I. Nakai, T. Tsubata, T. Himeda, and F. Nishikawa, *J. Solid State Chem.*, **133**, 587 (1997).
33. M. Moshkovich, M. Cojocaru, H. E. Gottlieb, and D. Aurbach, *J. Electroanal. Chem.*, **497**, 84 (2001).
34. K. Kanamura, *J. Power Sources*, **81-82**, 123 (1999).
35. A. D. Robertson and P. G. Bruce, *Chem. Mater.*, **15**, 1984 (2003).
36. N. Hayashi, H. Ikuta, and M. Wakihara, *J. Electrochem. Soc.*, **146**, 1351 (1999).
37. P. Strobel, A. Ibarra Palos, M. Anne, and F. Le Cras, *J. Mater. Chem.*, **10**, 429 (2000).